

This discussion paper is/has been under review for the journal Geoscientific Instrumentation, Methods and Data Systems (GID). Please refer to the corresponding final paper in GID if available.

# Experimental study of source of background noise in muon radiography using emulsion film detectors

R. Nishiyama<sup>1</sup>, S. Miyamoto<sup>1</sup>, and N. Naganawa<sup>2</sup>

<sup>1</sup>Earthquake Research Institute, The University of Tokyo, Tokyo, Japan

<sup>2</sup>Department of Physics, Graduate School of Science, Nagoya University, Nagoya, Japan

Received: 13 November 2013 – Accepted: 20 November 2013 – Published: 4 December 2013

Correspondence to: R. Nishiyama (nisiyama@eri.u-tokyo.ac.jp)

Published by Copernicus Publications on behalf of the European Geosciences Union.

BG study on muogrphy

R. Nishiyama et al.

Title Page

Abstract

Introduction

Conclusions

References

Tables

Figures

◀

▶

◀

▶

Back

Close

Full Screen / Esc

Printer-friendly Version

Interactive Discussion



## Abstract

We study the source of background noise in cosmic-ray muon radiography (muography) using emulsion film detectors. We claim that muography detectors should have a momentum separation function to reduce systematic errors due to non-signal particles with momenta less than  $2 \text{ GeV c}^{-1}$ . The origin of noise is expected to be electromagnetic components of air-showers or cosmic-ray muons scattered in topographic material. As a demonstration, we construct two types of detectors with different momentum thresholds and perform test measurements of an actual geoscientific target. The analysis of emulsion data is explained in detail, including film inefficiency compensation and momentum selection by applying an upper bound to the chi-square distribution to the data.

## 1 Introduction

Muon radiography (muography) is a non-invasive inspection technique that exploits the high penetration power of cosmic-ray muons (CR muons). Use of this technique has spread to a variety of fields, such as volcanology (e.g. Tanaka et al., 2007; Lesparre et al., 2012; Portal et al., 2013), and hydrology (e.g. Tanaka et al., 2011b). Muography technique is based on the measurement of the absorption of cosmic-ray muons inside the target material. The energy spectrum of CR muons and their interaction with matter have been extensively investigated, and the attenuation of muon flux can be used to derive the amount of matter present along the muon trajectories. The amount of matter is given in units of density times length (density-length,  $100 \text{ g cm}^{-2} = 1 \text{ m water equivalent} - \text{m.w.e.}$ ).

Muography of mountains has been performed by placing a position sensitive detector for minimum ionization particles (MIPs) at the foot of the target mountain. These measurements aim to detect muons that traverse the detector nearly horizontally. Since the flux of horizontal muons is approximately one-tenth to one-hundredth of that of vertical

GID

3, 649–677, 2013

BG study on  
muogrphy

R. Nishiyama et al.

Title Page

Abstract

Introduction

Conclusions

References

Tables

Figures

◀

▶

◀

▶

Back

Close

Full Screen / Esc

Printer-friendly Version

Interactive Discussion



muons, and it decreases drastically when passing through material, the number of signal muons is very small. Therefore, the background noise caused by non-signal particles must be excluded.

A requirement of signal muons is that they have to pass through the target material with a straight trajectory. These muons should have high momentum when they are detected. On the other hand, we assume that the following are sources of background particles: (1) electromagnetic components of air-showers and (2) CR muons deflected with large angles through the material. As discussed in the next section, most of these background particles have momentum less than  $2\text{ GeV c}^{-1}$ . These low-momentum particles are scattered into random directions by the material around the detector. They may pass through the detector by chance and may generate background noise.

Based on the above discussion, we conclude that a muography detector must have a momentum separation function to reduce systematic errors arising from low-momentum background particles. As a demonstration, we constructed two types of detectors with different momentum thresholds using emulsion films, and we performed a test measurement of an actual geoscientific target. In this paper, we describe the analysis method of the emulsion film data. Compensation for the film inefficiency is described in detail, since this process is crucial for converting the number of signals into the particle flux. Using the particle fluxes from the two detectors, we verify the existence of low-momentum background particles and we discuss their origin.

## 2 Signal and noise in muography

### 2.1 Signal muons

Muons are the most numerous charged particles at sea level (Beringer et al., 2012). They are produced high in the atmosphere from the decay of charged mesons (pions and kaons). Their energy and angular distribution reflects a convolution of their production spectrum, energy loss in the atmosphere and decay. The energy spectra of nearly

GID

3, 649–677, 2013

BG study on  
muogrphy

R. Nishiyama et al.

Title Page

Abstract

Introduction

Conclusions

References

Tables

Figures

◀

▶

◀

▶

Back

Close

Full Screen / Esc

Printer-friendly Version

Interactive Discussion



horizontal muons were investigated in detail in the MUTRON (Matsuno et al., 1984) and DEIS (Allkofer et al., 1985) experiments in the 1980s. In this study, we use the analytic formula of the muon energy spectrum developed by Matsuno et al. (1984). Although the formula does not take into account the rigidity cutoff due to the geomagnetism of the Earth, or the variation of solar activity, these effects affect the muon flux only in the GeV-range, and the variation is only 10%. The mean momentum of vertical muons is  $\sim 4 \text{ GeVc}^{-1}$  and that of nearly horizontal muons is  $\sim 10 \text{ GeVc}^{-1}$ . The background noise candidates, described in the next subsections, have typically lower momentum than the signal muons.

## 10 2.2 Electromagnetic components of air-showers

The electromagnetic components from electromagnetic cascades, which are initiated by the decay of neutral and charged mesons, can be sources of background noise in muography, since they are scattered into the detector from random directions. Electrons and positrons are most numerous near a critical energy (81 MeV in air). The total vertical intensity of electrons plus positions is roughly, 30, 6, and  $0.2 \text{ m}^{-2} \text{ s}^{-1} \text{ sr}^{-1}$  above 10, 100, and 1000 MeV respectively. A dedicated study (Golden et al., 1995) shows that the ratio of electrons plus positions to muons is as much as one-third at a few hundreds of MeV, and it decreases drastically to one-hundredth at 2 GeV. This precedent work implies that this component dominates the ionizing particles at ground level below critical energy (81 MeV). Unfortunately there are no sufficient experimental data for the angular dependence of the energy spectrum.

## 2.3 Scattered muons

Some CR muons are deflected with large angles in a target material due to multiple coulomb scattering and bremsstrahlung. These muons can also be a source of background noise in muography, since they lose their original information of direction through the material.

BG study on  
muogrphy

R. Nishiyama et al.

[Title Page](#)

[Abstract](#)

[Introduction](#)

[Conclusions](#)

[References](#)

[Tables](#)

[Figures](#)

[◀](#)

[▶](#)

[◀](#)

[▶](#)

[Back](#)

[Close](#)

[Full Screen / Esc](#)

[Printer-friendly Version](#)

[Interactive Discussion](#)



[Title Page](#)[Abstract](#)[Introduction](#)[Conclusions](#)[References](#)[Tables](#)[Figures](#)[◀](#)[▶](#)[◀](#)[▶](#)[Back](#)[Close](#)[Full Screen / Esc](#)[Printer-friendly Version](#)[Interactive Discussion](#)

### 3.2 Momentum measurement with ECC

When a charged particle passes through the material, the particle is scattered by the electric field of the nuclei (multiple coulomb scattering). A distribution of the scattering angle is described as a Gaussian probability function whose standard deviation is given by

$$\sigma_{\text{scatt}} = \frac{13.6 \text{ MeV}c^{-1}}{p\beta} \sqrt{\frac{t}{X_0}} \left\{ 1 + 0.038 \log \left( \frac{t}{X_0} \right) \right\}, \quad (1)$$

where  $p$  is the momentum,  $\beta$  the relative velocity to the speed of light, and  $t/X_0$  the thickness of the scatterer in radiation length (Lynch and Dahl, 1991).

The emulsion cloud chamber (ECC) is a modular structure made of a sandwich of passive material plates such as lead interleaved with emulsion film layers. Due to the very high position resolution of emulsion films, we can determine the momentum of the traversing particles by measuring small deflections of tracks caused by multiple coulomb scattering (De Serio et al., 2003). Since the typical angular resolution of tracks in an emulsion film is 5 mrad, we can identify scattering angles of  $1 \text{ GeV}c^{-1}$  particles in a 1 mm-thick lead plate.

## 4 Experimental setup and coordinate systems

We prepared two types of detectors using OPERA-type emulsion films to investigate the features of low-momentum noise particles. One is a stack of four emulsion films (quartet detector). The other is a stack of 20 emulsion films and nine 1 mm-thick lead plates (ECC detector). As discussed in Sect. 5.3.2, the momentum thresholds of these two detectors are  $0.2 \text{ GeV}c^{-1}$  (quartet) and  $2.0 \text{ GeV}c^{-1}$  (ECC), respectively. Schematic cross views of these detectors are shown in Fig. 3. We installed the detectors 500 m west of the summit of Mt. Showa-Shinzan in the Usu volcanic region in Hokkaido,

GID

3, 649–677, 2013

BG study on  
muogrphy

R. Nishiyama et al.

Title Page

Abstract

Introduction

Conclusions

References

Tables

Figures

◀

▶

◀

▶

Back

Close

Full Screen / Esc

Printer-friendly Version

Interactive Discussion



Japan. These detectors were faced toward Mt. Showa-Shinzan. Behind the detectors was another larger volcano, Mt. Usu. The exposure time was 168 days (21 November 2011 to 7 May 2012).

We employ a Cartesian coordinate system with the z-axis normal to the detector plane (Fig. 3c) to identify the track position and direction. The track orientation is represented by  $(\tan \theta_x, \tan \theta_y)$ , where  $\theta_x$  and  $\theta_y$  are the angles with respect to the film normal projected on the  $xz$  and  $yz$  planes, respectively. The inclination angle  $\theta = \sqrt{\theta_x^2 + \theta_y^2}$ , the angle between the track and the detector plane, is an important parameter, since the angular resolution and film efficiency depend strongly on  $\theta$ . While the ECC detector was placed vertically on the ground, we placed the quartet detector with a slant of  $\alpha = 11^\circ$  to the ground. Thus, in order to compare the results, the quartet coordinates  $(\theta_x^Q, \theta_y^Q)$  have to be transformed to the ECC coordinates  $(\theta_x, \theta_y)$  via the relation

$$\tan \theta_x^Q = \frac{\tan \theta_x}{\sin \alpha \tan \theta_y + \cos \alpha} \quad \tan \theta_y^Q = \frac{\cos \alpha \tan \theta_y - \sin \alpha}{\sin \alpha \tan \theta_y + \cos \alpha}. \quad (2)$$

15 In this coordinate system,  $\tan \theta_y > 0$  indicates particles coming from the front,  $\tan \theta_y < 0$  particles coming from the rear, and  $\tan \theta_y = 0$  horizontal particles, because almost all the cosmic particles travel downward. The thickness of the rock along the radial direction from the detector is shown in Fig. 4.

## 5 Analysis

## 20 5.1 Data acquisition and track reconstruction

After the films were developed, the tracks recorded in the emulsion films were read using European Scanning System (Arrabito et al., 2006). The readout system outputs the position, direction and linear density of the identified silver grains. Film-to-film alignment and track reconstruction were performed using the FEDRA framework (Tioukov



[Printer-friendly Version](#)

## Interactive Discussion

655

et al., 2006). We then applied several cuts to the reconstructed tracks. The efficiency for each cut is discussed in the subsequent section.

## 5.2 Track selection

### 5.2.1 Grain density cut

- 5 Minimum ionization particles (MIPs) are selected by removing tracks with an average grain density (number of AgBr grains on track) higher thresholds. The grain density is almost proportional to the ionizing power of the incident particles. This methodology has been established by several precedent studies. For instance, Toshito et al. (2004) succeeded in discriminating  $1.2 \text{ GeV c}^{-1}$  pions (MIPs) from  $1.2 \text{ GeV c}^{-1}$  protons (non-MIPs) in an accelerator beam.  
10

### 5.2.2 $\chi^2$ -cut

In order to select tracks with straight trajectories in the detector, we apply a chi-square cut based on deflection angle.  $\chi^2$  is defined as

$$\chi^2 = \sum \left( \frac{\Delta\theta_{R,i}^2}{\sigma_R^2} + \frac{\Delta\theta_{T,i}^2}{\sigma_T^2} \right), \quad (3)$$

- 15 where  $\Delta\theta_{R,i}$  and  $\Delta\theta_{T,i}$  are the deflection angles of tracks between the  $i$ th and  $(i+1)$ th films in radial and transverse coordinates, and  $\sigma_{R,L}$  are angular measurement errors, shown in Fig. 5. In the RL coordinate system, while the radial error increases with increasing  $\theta$ , the transverse error is less independent on  $\theta$  (De Serio et al., 2003). An example of the resultant  $\chi^2$  distribution is shown in Fig. 6. We select tracks with  
20  $p$  values  $\geq 0.01$  (1%).

<a href="#">Title Page</a>	
<a href="#">Abstract</a>	<a href="#">Introduction</a>
<a href="#">Conclusions</a>	<a href="#">References</a>
<a href="#">Tables</a>	<a href="#">Figures</a>
<a href="#">◀</a>	<a href="#">▶</a>
<a href="#">◀</a>	<a href="#">▶</a>
<a href="#">Back</a>	<a href="#">Close</a>
<a href="#">Full Screen / Esc</a>	
<a href="#">Printer-friendly Version</a>	
<a href="#">Interactive Discussion</a>	



## 5.2.3 Number of hits cut

We eliminate chance coincidences of tracks recorded during transportation using a cut based on the number of hits ( $n$ ) among the total number of films ( $N$ ). Figure 7 shows  $n$  distributions for selected almost-perpendicular tracks in the quartet detector ( $N = 4, 0 < \theta^Q < 0.2$ ) and the ECC detector ( $N = 20, 0 < \theta < 0.4$ ). Along with the number of hits distribution, we estimate the probability that the tracks recorded during transportation are linearly aligned by chance and mistakenly identified as signals (shaded histograms). In order to exclude these fake signals, we set the threshold as  $n \geq n_{\text{cut}}^Q = 3$  for the quartet detector, and  $n \geq n_{\text{cut}}^{\text{ECC}} = 5$  for the ECC detector.

- 5  
5.3 Efficiency study
- 10  
5.3.1 Film efficiency
- 15  
The film efficiency is defined as the probability of detecting a track in a film when a particle passes through it. Given the efficiency values of the quartet films,  $\epsilon_1, \epsilon_2, \epsilon_3$ , and  $\epsilon_4$ , the probability that tracks are found in at least  $n_{\text{cut}}^Q = 3$  of the total  $N = 4$  films can be expressed as

$$\epsilon_{\text{tot}}^Q = \epsilon_1 \epsilon_2 \epsilon_3 \epsilon_4 + (1 - \epsilon_1) \epsilon_2 \epsilon_3 \epsilon_4 + \epsilon_1 (1 - \epsilon_2) \epsilon_3 \epsilon_4 + \epsilon_1 \epsilon_2 (1 - \epsilon_3) \epsilon_4 + \epsilon_1 \epsilon_2 \epsilon_3 (1 - \epsilon_4). \quad (4)$$

The film efficiency values are estimated for several inclination ranges from the ratio of triplet-hit signals and quartet-hit signals:

$$\epsilon_i [\theta_{\min}^Q : \theta_{\max}^Q] = \frac{N_4 [\theta_{\min}^Q : \theta_{\max}^Q]}{N_{3,i} [\theta_{\min}^Q : \theta_{\max}^Q] + N_4 [\theta_{\min}^Q : \theta_{\max}^Q]}, \quad (5)$$

GID

3, 649–677, 2013

BG study on muogrphy

R. Nishiyama et al.

Title Page

Abstract

Introduction

Conclusions

References

Tables

Figures

◀

▶

◀

▶

Back

Close

Full Screen / Esc

Printer-friendly Version

Interactive Discussion



[Title Page](#)[Abstract](#)[Introduction](#)[Conclusions](#)[References](#)[Tables](#)[Figures](#)[◀](#)[▶](#)[◀](#)[▶](#)[Back](#)[Close](#)[Full Screen / Esc](#)[Printer-friendly Version](#)[Interactive Discussion](#)

where  $N_4[\theta_{\min}^Q : \theta_{\max}^Q]$  is the number of quartet-hit tracks with inclination within  $\theta_{\min}^Q \leq \theta^Q < \theta_{\max}^Q$ , and  $N_{3,i}$  is the number of tracks found in three films and not found in the  $i$ th film. As shown in Fig. 8a, the total efficiency  $\epsilon_{\text{tot}}^Q$  depends strongly on  $\theta$ .

For the ECC detector, the efficiency of one film is estimated by fitting the  $n$  distribution with a model function. We assume the single film efficiency  $\epsilon$  is a random variable following the beta distribution  $\text{beta}(\epsilon, a, b)$ , with mean and variance given by  $a/(a + b)$  and  $ab/(a + b)^2/(a + b + 1)$ . The expected  $n$  distribution can then be expressed as a beta-binomial function, a compound of beta and binomial distributions:

$$f(n|a, b) = \frac{N!}{(N-n)!n!} \frac{B(n+a, N-n+b)}{B(a,b)}, \quad (6)$$

where  $B(\dots)$  denotes the beta function. The model parameters  $(a, b)$  are determined by fitting the observed  $n$ -hit distribution with Eq. (6). We use the MINUIT package for this fitting. The total efficiency then becomes

$$\epsilon_{\text{tot}}^{\text{ECC}}[\theta_{\min} : \theta_{\max}] = \sum_{n=5}^{20} f(n|a[\theta_{\min} : \theta_{\max}], b[\theta_{\min} : \theta_{\max}]). \quad (7)$$

We show the film/total efficiency values of the ECC as a function of  $\theta$  in Fig. 8b. Although the single plate efficiency values are generally lower than the quartet values, the total efficiency is considerably higher than the quartet detector and is almost flat for  $\theta < 0.6$ . This stable, high efficiency is achieved due to the highly redundant films of the ECC detector.

### 5.3.2 Momentum thresholds

The surviving rate of the  $\chi^2$ -cut is estimated for a variety of momenta by a Monte Carlo simulation. Using random number generators, we generated deflection angles  $\Delta\theta_{R,L}$  for each gap in the detector and computed  $\chi_{\text{MC}}^2$  from Eq. (3). The deflection angles

were given as a combination of observational angular error and scattering angle in Eq. (1):

$$\Delta\theta_{R,L} = \zeta\sigma_{R,L} + \eta\sigma_{\text{scatt}}, \quad (8)$$

where  $\zeta$  and  $\eta$  are normal random variables with a mean of zero and a variance of one. The material and gap distance are taken into account in the  $t/X_0$  term in Eq. (1). Out of 10 000 tries, the percentage where the resultant  $\chi^2_{\text{MC}}$  meets the  $\chi^2$ -criterion ( $p$  value  $> 1\%$ ) is taken for the surviving rate at a given momentum  $e_{\text{mom}}(p)$ . Figure 9 shows the surviving probability as a function of momentum for the quartet and ECC detectors. While  $s(p)$  of the quartet detector approaches 90% at  $0.2\text{GeV}\text{c}^{-1}$ , the ECC detector rejects particles of this momentum. Thus, we can say that the momentum thresholds of the quartet and ECC detectors are  $0.2\text{GeV}\text{c}^{-1}$ , and  $2.0\text{GeV}\text{c}^{-1}$ , respectively.

## 5.4 Particle flux calculation

A particle flux from a solid angle spanned by  $D$ :  $[\tan\theta_{x,\min} : \tan\theta_{x,\max}, \tan\theta_{y,\min} : \tan\theta_{y,\max}]$  is derived from the number of selected tracks and the total efficiency values:

$$F^{Q,\text{ECC}} = \frac{1}{\int_D S \cos\theta T d\Omega} \left( \sum_i \frac{N[\theta_{i,\min} : \theta_{i,\max}]}{\epsilon_{\text{tot}}[\theta_{i,\min} : \theta_{i,\max}]} \right), \quad (9)$$

where  $N[\theta_{i,\min} : \theta_{i,\max}]$  denotes the number of selected tracks in the  $i$ th inclination range,  $S$  the area of the film in the analysis,  $\Omega$  the solid angle, and  $T$  the exposure time.

## 5.5 Simulated muon flux

For comparison with the observed particle fluxes, we calculate the expected values of the muon flux for a variety of values of topographic density  $\rho_{\text{sim}}$ . The calculation

[Title Page](#)

[Abstract](#)

[Introduction](#)

[Conclusions](#)

[References](#)

[Tables](#)

[Figures](#)

[◀](#)

[▶](#)

[◀](#)

[▶](#)

[Back](#)

[Close](#)

[Full Screen / Esc](#)

[Printer-friendly Version](#)

[Interactive Discussion](#)



was performed by subdividing the view into small sections and summing the integrated theoretical muon energy spectrum above the cutoff energies:

$$F^{\text{SIM}} = \frac{1}{\sum_{x,y} S \cos \theta_{x,y} T \Delta \Omega} \left\{ \sum_{x,y} S \cos \theta_{x,y} T \Delta \Omega_{x,y} \int_{E_{\text{cut}}(X_{x,y})}^{\infty} f_{\mu}(\vartheta_{x,y}, E) dE \right\}. \quad (10)$$

Here,  $\Delta \Omega_{xy}$  and  $\vartheta_{x,y}$  are the solid angle and the zenith angle for the subdivided view with intervals of  $[\Delta \tan \theta_x, \Delta \tan \theta_y] = [0.01, 0.01]$ . The energy cutoff  $E_{\text{cut}}$  value for a given density-length is taken from the muon range table (Groom et al., 2001). The density-length of the rock along the radial direction for the subdivided view was given by  $X_{x,y} = \rho_{\text{sim}} \times$  (thickness of rock).

## 5.6 Results

We summarize the results in Table 1. We estimate the particle fluxes ( $F^{\text{Q,ECC}}$ ) for three angular domains, in which the rock thickness along the radial directions ranges in (a) 70–469 m, (b) 432–1100 m, and (c) 907–3879 m, as shown in Fig. 4. Using the observed fluxes, we estimate the average density of rock in each view by comparing them with the simulated flux (Fig. 10). The quartet detector yields an average density of  $1.18^{+0.04}_{-0.04}$ ,  $0.76^{+0.05}_{-0.05}$ , and  $0.23^{+0.02}_{-0.02}$  g cm<sup>-3</sup> for domains (a), (b), and (c), respectively. The ECC detector yields  $2.33^{+0.12}_{-0.10}$  and  $2.00^{+0.23}_{-0.17}$  g cm<sup>-3</sup> for domains (a) and (b). For domain (c), we could not determine the average density due to the lack of statistics.

For each domain (a), (b), and (c), the particle flux estimated from the quartet detector is much higher than that from the ECC detector. Considering the different momentum thresholds for the two detectors, this difference in flux arises from the low momenta particles in  $0.2 \text{ GeV c}^{-1} < p < 2 \text{ GeV c}^{-1}$ . While the density values determined from the ECC detector are consistent with the density of typical volcanic rocks, the density values determined from the quartet detector are significantly low. This fact suggests that while the ECC detects only the signal muons, the quartet detector is affected by contamination from other low-momentum particles.

[Title Page](#)

[Abstract](#)

[Introduction](#)

[Conclusions](#)

[References](#)

[Tables](#)

[Figures](#)

[◀](#)

[▶](#)

[◀](#)

[▶](#)

[Back](#)

[Close](#)

[Full Screen / Esc](#)

[Printer-friendly Version](#)

[Interactive Discussion](#)



## 6 Discussion and conclusion

This study confirms that the source of background noise in muon radiography is charged particles with momenta  $< 2\text{ GeVc}^{-1}$ . It also demonstrates that a momentum discerning detector, like an ECC detector, can reduce the contribution from background noise to negligible levels.

We now compare our conclusion with some earlier studies of the background noise particles in muon radiography. Tanaka et al. (2011a) discussed false muon tracks which arise when several particles accidentally hit several counter planes at the same time within the time resolution of the electronic muon detector. This type of noise is negligible in emulsion detectors because emulsion detectors have high position and direction resolution, and the frequency of random coincidence of the tracks is lowered to negligible levels as a result of the number of hits cut. Lesparre et al. (2012) discusses the contamination from electromagnetic components of air-shower particles. They inserted 24 mm-thick of iron plates between the counter planes to stop  $e^+/e^-$  particles with kinetic energies  $< 108.3\text{ MeV}$ . In our study, the quartet detector also excludes particles in this energy range; however, we still see an excess of particle flux. This difference should be further studied with consideration of detector dependence problems.

It has not yet been determined whether low-momenta noise particles consist of electromagnetic components or scattered muons, since our ECC detector does not identify the type of particle because the thickness of the absorbing material in the detector is not sufficient for electromagnetic calorimetry. Miyamoto (2013) used emulsion detectors like our quartet detector in a cave in Mt. Unzen and detected a significant excess of the near-horizontal particle flux, although most of the  $e^+/e^-$  particles seemed to be absorbed in the overburden rocks of thickness more than 10 m. This suggests that the background noise contains non-electromagnetic components. We believe this subject should be further studied both numerically and experimentally. Numerical studies should include a Monte Carlo simulation considering particle scattering in the atmosphere and topography, and particle deflection in the geomagnetic

GID

3, 649–677, 2013

BG study on  
muogrphy

R. Nishiyama et al.

[Title Page](#)

[Abstract](#)

[Introduction](#)

[Conclusions](#)

[References](#)

[Tables](#)

[Figures](#)

◀

▶

◀

▶

[Back](#)

[Close](#)

[Full Screen / Esc](#)

[Printer-friendly Version](#)

[Interactive Discussion](#)



[Title Page](#)[Abstract](#)[Introduction](#)[Conclusions](#)[References](#)[Tables](#)[Figures](#)[◀](#)[▶](#)[◀](#)[▶](#)[Back](#)[Close](#)[Full Screen / Esc](#)[Printer-friendly Version](#)[Interactive Discussion](#)

field of the Earth. There are some pioneering works of such large-scale computation. For instance, Honda et al. (2004) performed atmospheric neutrino flux calculations in three-dimensional space with IGRF geomagnetic model for neutrino oscillation experiments. Béné et al. (2013) attempted to quantify the amount of accidental coincidences produced in the detector by air-shower induced particles. As an example of an experimental approach, we believe that an underwater measurement is feasible, where the flux of the electromagnetic components is negligible and the density of overburden material above the detector is given beforehand.

**Acknowledgements.** The authors wish to thank M. Nakamura and his colleagues for their support in preparing and developing the emulsion films. Installation of the emulsion detectors was supported by H. Oshima and T. Maekawa from Hokkaido University. Beautification Escort Staff (BES) at Shikotsu-Toya National Park provided us with a site for our observation. We are grateful to C. Bozza for his continuing support in the use of the European Scanning System. We acknowledge with gratitude the tremendous support in the use of the FEDRA framework by V. Tioukov. We thank H. K. M. Tanaka and S. Okubo for their encouragement and valuable discussions. During this work, one of the authors (R. Nishiyama) was supported by JSPS Fellowship (24-9317).

## References

- Agostinelli, S., Allison, J., Amako, K., Apostolakis, J., Araujo, H., Arce, P., Asai, M., Axen, D., Banerjee, S., Barrand, G., Behner, F., Bellagamba , L., Boudreau, J., Broglia, L., Brunengo, A., Burkhardt, H., Chauvie, S., Chuma, J., Chytracek, R., Cooperman, G., Cosmo, G., Degtyare, S., Giani, S., Giannitrapani, R., Gibin, D., Gómez Cadenas, J. J., González, I., Gracia Abril, G., Greeniaus, G., Greiner, W., Grichine, V., Grossheim, A., Guatelli, S., Gumplinger, P., Hamatsu, R., Hashimoto, K., Hasui, H., Heikkinen, A., Howard, A., Ivanchenko, V., Johnson, A., Jones, F. W., Kallenbach, J., Kanaya, N., Kawabata, M., Kawabata, Y., Kawaguti, M., Kelner, S., Kent, P., Kimura, A., Kodama, T., Kokoulin, R., Kossov, M., Kurashige, H., Lamanna, E., Lampén, T., Lara, V., Lefebure, V., Le, E., Minamimoto, K., Mora de Freitas, P., Morita, Y., Murakami, K., Nagamatu, M., Nartallo, R., Nieminen, P., Nishimura, T., Ohtsubo, K., Okamura, M., O'Neale, S., Oohata , Y., Paech, K., Perl, J., Pfeiffer, A., Pia, M. G.,

**BG study on muogrphy**

R. Nishiyama et al.

Ranjard, F., Rybin, A., Sadilov, S., Di Salvo, E., Santin, G., Sasaki, T., Savvas, N., Sawada, Y., Scherer, S., Sei, S., Sirotenko, V., Smith, D., Starkov, N., Stoecker, H., Sulkimo, J., Takahata, M., Tanaka, S., Tcherniaev, E., Safai Tehrani, E., Tropeano, M., Truscott, P., Uno, H., Urban, L., Urban, P., Verderi, M., Walkden, A., Wander, W., Weber, H., Wellisch, J. P., Wenaus, T., Williams, D. C., Wright, D., Yamada, T., Yoshida, H., and Zschiesche, D.: GEANT4 – a simulation toolkit, Nucl. Instrum. Meth. A, 506, 250–303, 2003. 653

Allkofer, O., Bella, G., Dau, W., Jokisch, H., Klemke, G., Oren, Y., and Uhr, R.: Cosmic ray muon spectra at sea-level up to 10 TeV, Nucl. Phys. B, 259, 1–18, 1985. 652

Arrabito, L., Barbuto, E., Bozza, C., Buontempo, S., Consiglio, L., Coppola, D., Cozzi, M., Damet, J., D'Ambrosio, N., De Lellis, G., De Serio, M., Di Capua, F., Di Ferdinando, D., Di Marco, D., Esposito, L. S., Giacomelli, G., Grella, G., Hauger, M., Juget, F., Kreslo, I., Giorgini, M., Ieva, M., Laktineh, I., Manai, K., Mandrioli, G., Marotta, A., Manzoor, S., Migliozi, P., Monacelli, P., Muciaccia, M. T., Pastore, A., Patrizii, L., Pistillo, C., Pozzato, M., Royole-Degieux, P., Romano, G., Rosa, G., Savvinov, N., Schembri, A., Scotto Lavina, L., Simone, S., Sioli, M., Sirignan, C., Sirri, G., Sorrentino, G., Strolin, P., Tioukov, V., and Waelchli, T.: Hardware performance of a scanning system for high speed analysis of nuclear emulsions, Nucl. Instrum. Meth. A, 568, 578–587, 2006. 653, 655

Béné, S., Boivin, P., Busato, E., Cârloganu, C., Combaret, C., Dupieux, P., Fehr, F., Gay, P., Labazuy, P., Laktineh, I., Lénat, J.-F., Miallier, D., Mirabito, L., Niess, V., Portal, A., and Vulpescu, B.: Air shower simulation for background estimation in muon tomography of volcanoes, Geosci. Instrum. Method. Data Syst., 2, 11–15, doi:10.5194/gi-2-11-2013, 2013. 662

Beringer, J., Arguin, J.-F., Barnett, R. M., Copic, K., Dahl, O., Groom, D. E., Lin, C.-J., Lys, J., Murayama, H., Wohl, C. G., Yao, W.-M., Zyla, P. A., Amsler, C., Antonelli, M., Asner, D. M., Baer, H., Band, H. R., Basaglia, T., Bauer, C. W., Beatty, J. J., Belousov, V. I., Bergren, E., Bernardi, G., Bertl, W., Bethke, S., Bichsel, H., Biebel, O., Blucher, E., Blusk, S., Brooijmans, G., Buchmueller, O., Cahn, R. N., Carena, M., Ceccucci, A., Chakraborty, D., Chen, M.-C., Chivukula, R. S., Cowan, G., D'Ambrosio, G., Damour, T., de Florian, D., de Gouvêa, A., DeGrand, T., de Jong, P., Dissertori, G., Dobrescu, B., Doser, M., Drees, M., Edwards, D. A., Eidelman, S., Erler, J., Ezhela, V. V., Fettscher, W., Fields, B. D., Foster, B., Gaisser, T. K., Garren, L., Gerber, H.-J., Gerbier, G., Gherghetta, T., Golwala, S., Goodman, M., Grab, C., Gritsan, A. V., Grivaz, J.-F., Grünewald, M., Gurtu, A., Gutsche, T., Haber, H. E., Hagiwara, K., Hagmann, C., Hanhart, C., Hashimoto, S., Hayes, K. G., Heffner, M., Heltsley, B., Hernández-Rey, J. J., Hikasa, K., Höcker, A., Holder, J., Holtkamp, A., Huston, J., Jackson,

[Title Page](#)[Abstract](#)[Introduction](#)[Conclusions](#)[References](#)[Tables](#)[Figures](#)[◀](#)[▶](#)[◀](#)[▶](#)[Back](#)[Close](#)[Full Screen / Esc](#)[Printer-friendly Version](#)[Interactive Discussion](#)

BG study on  
muography

R. Nishiyama et al.

[Title Page](#)[Abstract](#)[Introduction](#)[Conclusions](#)[References](#)[Tables](#)[Figures](#)[◀](#)[▶](#)[◀](#)[▶](#)[Back](#)[Close](#)[Full Screen / Esc](#)[Printer-friendly Version](#)[Interactive Discussion](#)

J. D., Johnson, K. F., Junk, T., Karlen, D., Kirkby, D., Klein, S. R., Klempert, E., Kowalewski, R. V., Krauss, F., Kreps, M., Krusche, B., Kuyanov, Yu. V., Kwon, Y., Lahav, O., Laiho, J., Langacker, P., Liddle, A., Ligeti, Z., Liss, T. M., Littenberg, L., Lugovsky, K. S., Lugovsky, S. B., Mannel, T., Manohar, A. V., Marciano, W. J., Martin, A. D., Masoni, A., Matthews, J., Millstead, D., Miquel, R., Mönig, K., Moortgat, F., Nakamura, K., Narain, M., Nason, P., Navas, S., Neubert, M., Nevski, P., Nir, Y., Olive, K. A., Pape, L., Parsons, J., Patrignani, C., Peacock, J. A., Petcov, S. T., Piepke, A., Pomarol, A., Punzi, G., Quadt, A., Raby, S., Raffelt, G., Ratcliff, B. N., Richardson, P., Roesler, S., Rolli, S., Romaniouk, A., Rosenberg, L. J., Rosner, J. L., Sachrajda, C. T., Sakai, Y., Salam, G. P., Sarkar, S., Sauli, F., Schneider, O., Scholberg, K., Scott, D., Seligman, W. G., Shaevitz, M. H., Sharpe, S. R., Silari, M., Sjöstrand, T., Skands, P., Smith, J. G., Smoot, G. F., Spanier, S., Spieler, H., Stahl, A., Stanev, T., Stone, S. L., Sumiyoshi, T., Syphers, M. J., Takahashi, F., Tanabashi, M., Terning, J., Titov, M., Tkachenko, N. P., Törnqvist, N. A., Tovey, D., Valencia, G., van Bibber, K., Venanzoni, G., Vincter, M. G., Vogel, P., Vogt, A., Walkowiak, W., Walter, C. W., Ward, D. R., Watari, T., Weiglein, G., Weinberg, E. J., Wiencke, L. R., Wolfenstein, L., Womersley, J., Woody, C. L., Workman, R. L., Yamamoto, A., Zeller, G. P., Zenin, O. V., Zhang, J., Zhu, R.-Y., Harper, G., Lugovsky, V. S., and Schaffner, P.: Review of particle physics, Phys. Rev. D, 86, 010001, doi:10.1103/PhysRevD.86.010001, 2012. 651

De Serio, M., Ieva, M., Simone, S., Giorgini, M., Sioli, M., Sirri, G., Buontempo, S., D'Ambrosio, N., De Lellis, G., De Rosa, G., Barbuto, E., Bozza, C., and Sirignano, C.: Momentum measurement by the angular method in the Emulsion Cloud Chamber, Nucl. Instrum. Meth. A, 512, 539–545, 2003. 654, 656

Golden, R., Stephens, S., Stochaj, S., Webber, W., Brunetti, M., Codino, A., Grimani, C., Menichelli, M., Salvatori, I., De Pascale, M. P., Morselli, A., Picozza, P., Basini, G., Bonfigli, F., Brancaccio, F. M., Ricci, M., Ormes, J. F., Streitmatter, R. E., Papini, P., Piccardi, S., and Spillantini, P.: Measurement of the energy spectra of cosmic ray electron component and protons at ground level, J. Geophys. Res., 100, 23515–23523, 1995. 652

Groom, D. E., Mokhov, N. V., and Striganov, S. I.: Muon Stopping Power and Range Tables 10 MeV–100 TeV, Atom. Data Nucl. Data Tab., 78, 183–356, 2001. 660

Honda, M., Kajita, T., Kasahara, K., and Midorikawa, S.: New calculation of the atmospheric neutrino flux in a three-dimensional scheme, Phys. Rev. D, 70, 043008, doi:10.1103/PhysRevD.70.043008, 2004. 662

**BG study on muogrphy**

R. Nishiyama et al.

[Title Page](#)[Abstract](#)[Introduction](#)[Conclusions](#)[References](#)[Tables](#)[Figures](#)[◀](#)[▶](#)[◀](#)[▶](#)[Back](#)[Close](#)[Full Screen / Esc](#)[Printer-friendly Version](#)[Interactive Discussion](#)

Lesparre, N., Gibert, D., Marteau, J., Komorowski, J.-C., Nicollin, F., and Coutant, O.: Density muon radiography of La Soufrière of Guadeloupe volcano: comparison with geological, electrical resistivity and gravity data, *Geophys. J. Int.*, 190, 1008–1019, 2012. 650, 661

Lynch, G. R. and Dahl, O. I.: Approximations to multiple Coulomb scattering, *Nucl. Instrum. Meth. B*, 58, 6–10, 1991. 654

Matsuno, S., Kajino, F., Kawashima, Y., Kitamura, T., Mitsui, K., Muraki, Y., Ohashi, Y., Okada, A., Suda, T., Minorikawa, Y., Kobayakawa, K., Kamiya, Y., Nakamura, I., and Takahashi, T.: Cosmic-ray muon spectrum up to 20 TeV at 89° zenith angle, *Phys. Rev. D*, 29, 1–23, doi:10.1103/PhysRevD.29.1, 1984. 652

10 Miyamoto, S.: Nuclear emulsion: the review of the recent observations and the development of technologies, in: *Muon and Neutrino Radiography*, Tokyo, Japan, available at: <http://www.eri.u-tokyo.ac.jp/ht/MNR13/>, last access: December 2013. 661

Morishima, K. and Nakano, T.: Development of a new automatic nuclear emulsion scanning system, S-UTS, with continuous 3-D tomographic image read-out, *J. Instr.*, 5, P04011, doi:10.1088/1748-0221/5/04/P04011, 2010. 653

15 Nakamura, T., Ariga, A., Ban, T., Fukuda, T., Fukuda, T., Fujioka, T., Furukawa, T., Hamada, K., Hayashi, H., Hiramatsu, S., Hoshino, K., Kawada, J., Koike, N., Komatsu, M., Matsuoaka, H., Miyamoto, S., Miyanishi, K., Miyanishi, M., Morishima, K., Nada, H., Naganawa, N., Nakano, T., Narita, K., Natsume, M., Niwa, K., Nonaka, N., Park, B. D., Sato, O., Takahashi, S., Toshito, T., Uetake, T., Nakamura, M., Kuwabara, K., Nishiyama, S., Nonoyama, Y., and Kodama, K.: The OPERA film: new nuclear emulsion for large-scale, high-precision experiments, *Nucl. Instrum. Meth. A*, 556, 80–86, 2006. 653

20 Portal, A., Labazuy, P., Lénat, J.-F., Béné, S., Boivin, P., Busato, E., Cârloganu, C., Combaret, C., Dupieux, P., Fehr, F., Gay, P., Laktineh, I., Miallier, D., Mirabito, L., Niess, V., and Vulpescu, B.: Inner structure of the Puy de Dôme volcano: cross-comparison of geophysical models (ERT, gravimetry, muon imaging), *Geosci. Instrum. Method. Data Syst.*, 2, 47–54, doi:10.5194/gi-2-47-2013, 2013. 650

25 Tanaka, H., Nakano, T., Takahashi, S., Yoshida, J., and Niwa, K.: Development of an emulsion imaging system for cosmic-ray muon radiography to explore the internal structure of a volcano, Mt. Asama, *Nucl. Instrum. Meth. A*, 575, 489–497, 2007. 650

30 Tanaka, H., Uchida, T., and Tanaka, M.: Newly Developed Multi-Layered Muon Detection System for the Next Generation of Muon Radiography, in: *EGU General Assembly*, EGU2011-2932, Vienna, Austria, 2011a. 661

- Tanaka, H. K., Miyajima, H., Kusagaya, T., Taketa, A., Uchida, T., and Tanaka, M.: Cosmic muon imaging of hidden seismic fault zones: rainwater permeation into the mechanical fractured zones in Itoigawa–Shizuoka Tectonic Line, Japan, *Earth Planet. Sc. Lett.*, 306, 156–162, 2011b. 650
- 5 Tioukov, V., Kreslo, I., Petukhov, Y., and Sirri, G.: The FEDRA – Framework for emulsion data reconstruction and analysis in the OPERA experiment, *Nucl. Instrum. Meth. A*, 559, 103–105, 2006. 655
- Toshito, T., Ariga, A., Ban, T., Hoshino, K., Komatsu, M., Naganawa, N., Nakamura, M., Nakamura, T., Nakano, T., and Niwa, K.:  $\pi/p$  separation at  $1.2 \text{ GeV c}^{-1}$  by an emulsion cloud chamber, *Nucl. Instrum. Meth. A*, 516, 436–439, 2004. 656

<a href="#">Title Page</a>	
<a href="#">Abstract</a>	<a href="#">Introduction</a>
<a href="#">Conclusions</a>	<a href="#">References</a>
<a href="#">Tables</a>	<a href="#">Figures</a>
<a href="#">◀</a>	<a href="#">▶</a>
<a href="#">◀</a>	<a href="#">▶</a>
<a href="#">Back</a>	<a href="#">Close</a>
<a href="#">Full Screen / Esc</a>	
<a href="#">Printer-friendly Version</a>	
<a href="#">Interactive Discussion</a>	



Quartet detector: $S = 27 \text{ cm}^2, T = 1.45 \times 10^7 \text{ s}$				
inclination range: $\theta^Q$	domain (a)	domain (b)	domain (c)	efficiency (%): $\epsilon_{\text{tot}}^Q$
0–0.126	151	71	–	$91.5 \pm 2.0$
0.126–0.200	168	34	–	$90.2 \pm 1.8$
0.200–0.262	1	3	27	$72.4 \pm 1.7$
0.262–0.317	–	–	20	$62.0 \pm 1.4$
0.317–0.368	–	–	28	$54.5 \pm 1.4$
0.368–0.416	–	–	27	$50.3 \pm 1.5$
0.416–0.461	–	–	2	$45.4 \pm 1.5$
total statistics	320	108	104	
flux: $F^Q(\text{cm}^{-2} \text{ sr}^{-1} \text{ s}^{-1})$	$(2.97 \pm 0.17) \times 10^{-5}$	$(8.25 \pm 0.80) \times 10^{-6}$	$(1.19 \pm 0.12) \times 10^{-5}$	
estimated density ( $\text{g cm}^{-3}$ )	$1.18^{+0.04}_{-0.04}$	$0.76^{+0.05}_{-0.05}$	$0.22^{+0.02}_{-0.02}$	
ECC detector: $S = 27 \text{ cm}^2, T = 1.45 \times 10^7 \text{ s}$				
inclination range: $\theta$	domain (a)	domain (b)	domain (c)	efficiency (%): $\epsilon_{\text{tot}}^{\text{ECC}}$
0–0.200	–	15	2	> 98.4
0.200–0.317	27	2	–	$98.4 \pm 0.7$
0.317–0.416	75	–	–	$94.4 \pm 0.3$
total statistics	102	17	2	
flux: $F^{\text{ECC}}(\text{cm}^{-2} \text{ sr}^{-1} \text{ s}^{-1})$	$(8.23 \pm 0.81) \times 10^{-6}$	$(1.15 \pm 0.28) \times 10^{-6}$	too low statistics	
estimated density ( $\text{g cm}^{-3}$ )	$2.33^{+0.12}_{-0.10}$	$2.00^{+0.23}_{-0.17}$	too low statistics	

Title Page

Abstract

Introduction

Conclusions

References

Tables

Figures

◀

▶

◀

▶

Back

Close

Full Screen / Esc

Printer-friendly Version

Interactive Discussion



**BG study on muogrphy**

R. Nishiyama et al.

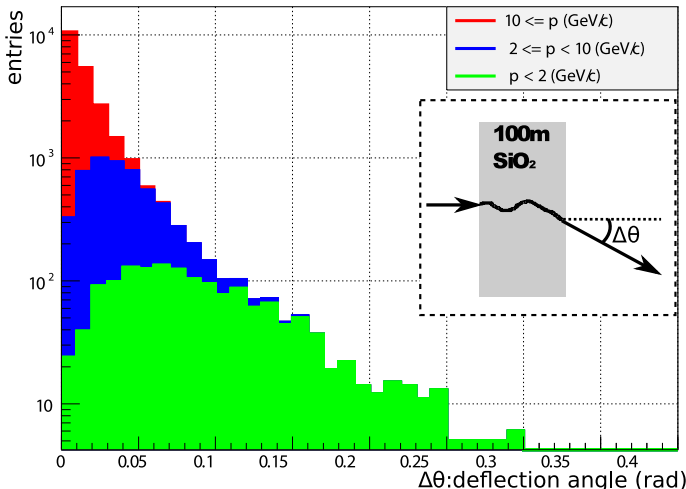


**Fig. 1.** Deflection angles of CR muons after passing through 100 m thickness of quartz (simulated using GEANT4). The injection momenta are adjusted to the CR muon momentum spectrum for a zenith angle of 80°. The histogram is classified into three color parts based on the momenta of the ejected muons, green:  $p_{\text{out}} < 2 \text{ GeV}c^{-1}$ , blue:  $2 \text{ GeV}c^{-1} \leq p_{\text{out}} < 10 \text{ GeV}c^{-1}$ , and red:  $10 \text{ GeV}c^{-1} < p_{\text{out}}$ .

<a href="#">Title Page</a>	<a href="#">Abstract</a>	<a href="#">Introduction</a>
<a href="#">Conclusions</a>	<a href="#">References</a>	
<a href="#">Tables</a>	<a href="#">Figures</a>	
<a href="#">◀</a>	<a href="#">▶</a>	
<a href="#">◀</a>	<a href="#">▶</a>	
<a href="#">Back</a>	<a href="#">Close</a>	
<a href="#">Full Screen / Esc</a>		
<a href="#">Printer-friendly Version</a>		
<a href="#">Interactive Discussion</a>		



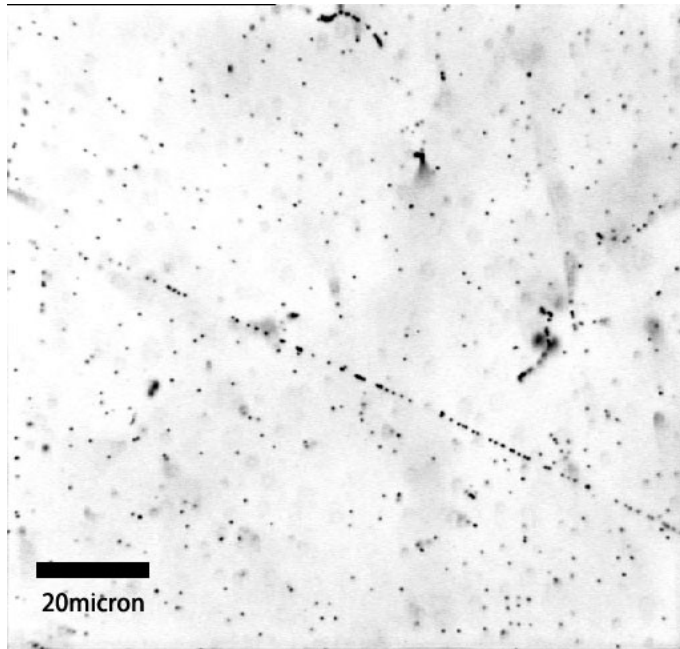


**Fig. 2.** Microscopic image of developed nuclear emulsion film.

## BG study on muogrpahy

R. Nishiyama et al.

[Title Page](#)

[Abstract](#)

[Introduction](#)

[Conclusions](#)

[References](#)

[Tables](#)

[Figures](#)

[◀](#)

[▶](#)

[◀](#)

[▶](#)

[Back](#)

[Close](#)

[Full Screen / Esc](#)

[Printer-friendly Version](#)

[Interactive Discussion](#)



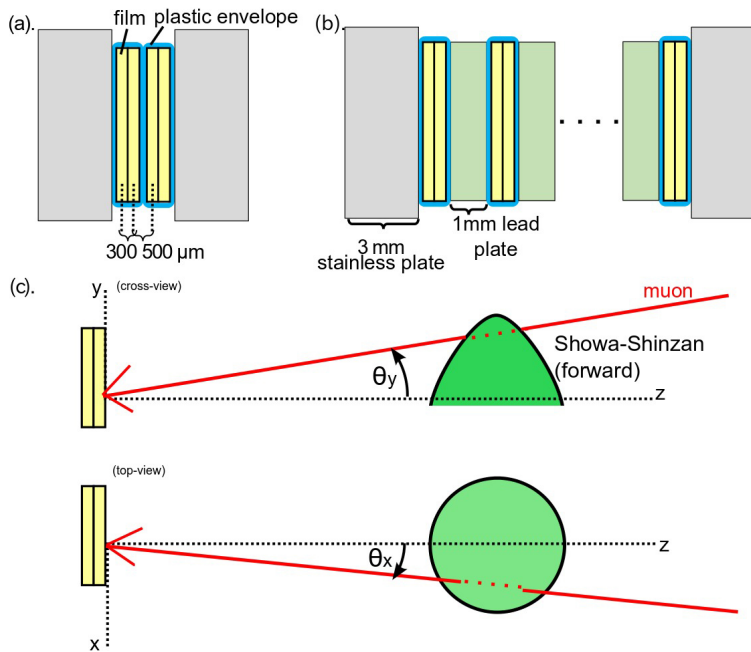


**Fig. 3.** Schematic cross views of two types of emulsion detectors. **(a)** Quartet detector: emulsion films, packed in twos in plastic light shielding envelopes stacked between 3 mm-thick stainless steel plates to ensure planarity. **(b)** ECC detector: ten envelopes and nine 1 mm-thick lead plates interleaved between 3 mm-thick stainless steel plates. **(c)** Emulsion coordinate system for identifying the position and direction of particles.

# BG study on muography

R. Nishiyama et al.

Title Page

## Abstract

Introduction

## Conclusion

## References

Tables

## Figures

1

1

1

1

Back

**Close**

Full Screen / Esc

[Printer-friendly Version](#)

## Interactive Discussion



**BG study on muogrphy**

R. Nishiyama et al.

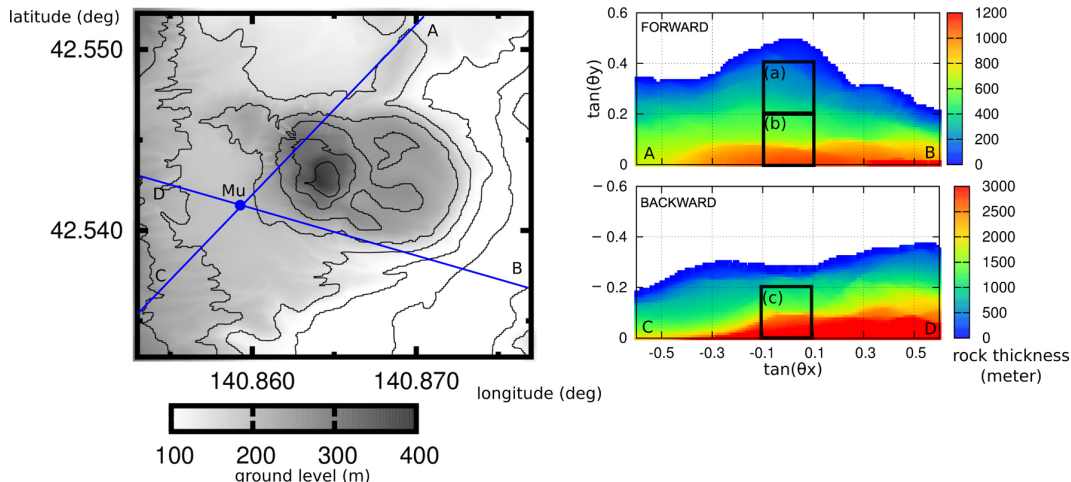


**Fig. 4.** Topological map of Showa-Shinzan Lava Dome, Usu, Japan. “Mu” shows the position of our emulsion detectors. The observations ranges of the muon detector are given by  $\angle \text{AMB}$  (forward) and  $\angle \text{CMD}$  (backward). The thickness of the material along the radial directions are represented in the two color contour maps to the right.

<a href="#">Title Page</a>	<a href="#">Abstract</a>	<a href="#">Introduction</a>
<a href="#">Conclusions</a>	<a href="#">References</a>	
<a href="#">Tables</a>	<a href="#">Figures</a>	
<a href="#">Discussion Paper</a>		
<a href="#">◀</a>	<a href="#">▶</a>	
<a href="#">◀</a>	<a href="#">▶</a>	
<a href="#">Back</a>	<a href="#">Close</a>	
<a href="#">Full Screen / Esc</a>		
<a href="#">Printer-friendly Version</a>		
<a href="#">Interactive Discussion</a>		



**BG study on muogrphy**

R. Nishiyama et al.

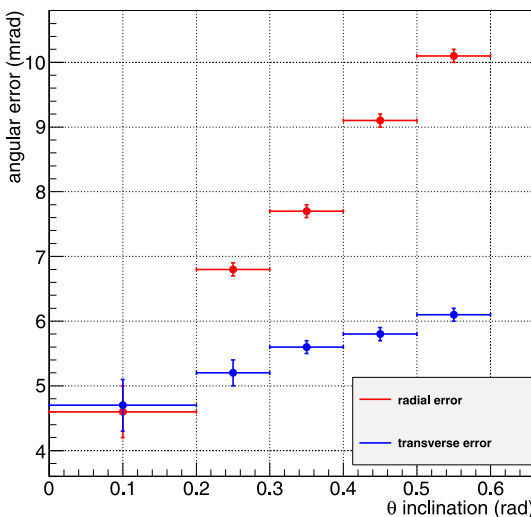


**Fig. 5.** Angular resolutions in the radial (red) and transverse (blue) coordinates. The horizontal axis represents the angle between a track and the normal direction of the detection plane (inclination:  $\theta$ ).

## BG study on muogrphy

R. Nishiyama et al.

[Title Page](#)

[Abstract](#)

[Introduction](#)

[Conclusions](#)

[References](#)

[Tables](#)

[Figures](#)

◀

▶

◀

▶

[Back](#)

[Close](#)

[Full Screen / Esc](#)

[Printer-friendly Version](#)

[Interactive Discussion](#)

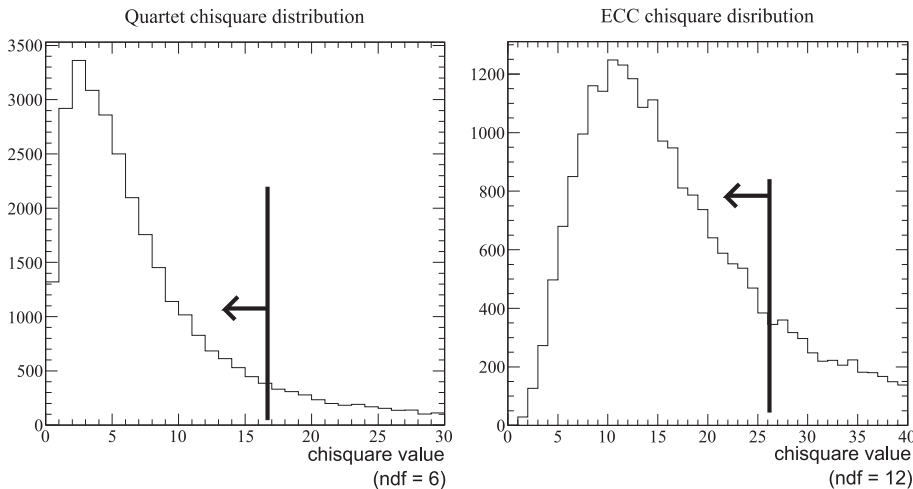


**Fig. 6.** Example resultant distributions of  $\chi^2$  values for the quartet detector (left: ndf = 6) and ECC detector (right: ndf = 12). The solid vertical line represents the upper bound we used based on the chi-square criterion ( $p$  value > 1%).

**BG study on muogrpahy**

R. Nishiyama et al.

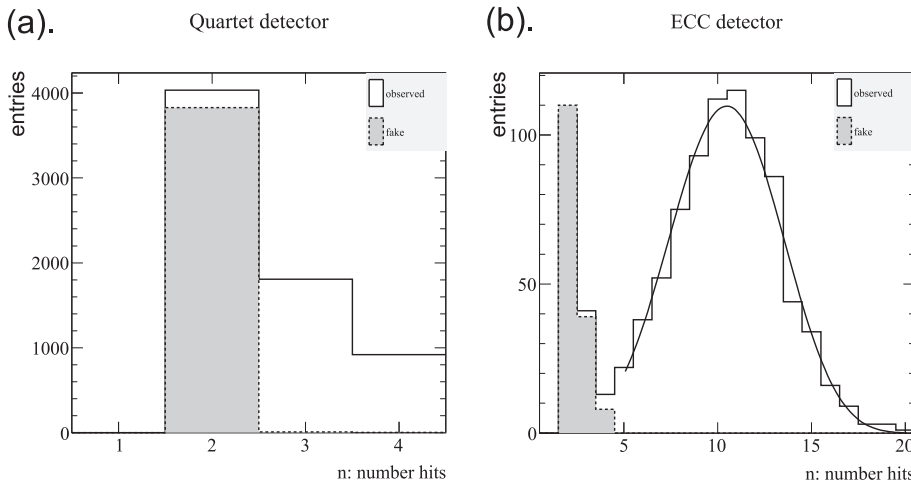


**Fig. 7. (a)** number of hits distribution among the four films in the quartet detector for tracks with inclination  $0.2 \leq \theta^Q \leq 0.262$ . The shaded histogram shows the probability that the tracks recorded during transportation are linearly aligned by chance and mistakenly identified as signals (fake signals). **(b)** number of hits distribution among the 20 films in the ECC detector for tracks with inclination  $0.2 \leq \theta \leq 0.317$ , fitted with a beta-binomial distribution.

<a href="#">Title Page</a>	<a href="#">Abstract</a>	<a href="#">Introduction</a>
<a href="#">Conclusions</a>	<a href="#">References</a>	
<a href="#">Tables</a>	<a href="#">Figures</a>	
<a href="#">◀</a>	<a href="#">▶</a>	
<a href="#">◀</a>	<a href="#">▶</a>	
<a href="#">Back</a>	<a href="#">Close</a>	
<a href="#">Full Screen / Esc</a>		

<a href="#">Printer-friendly Version</a>
<a href="#">Interactive Discussion</a>



**BG study on muogrpahy**

R. Nishiyama et al.

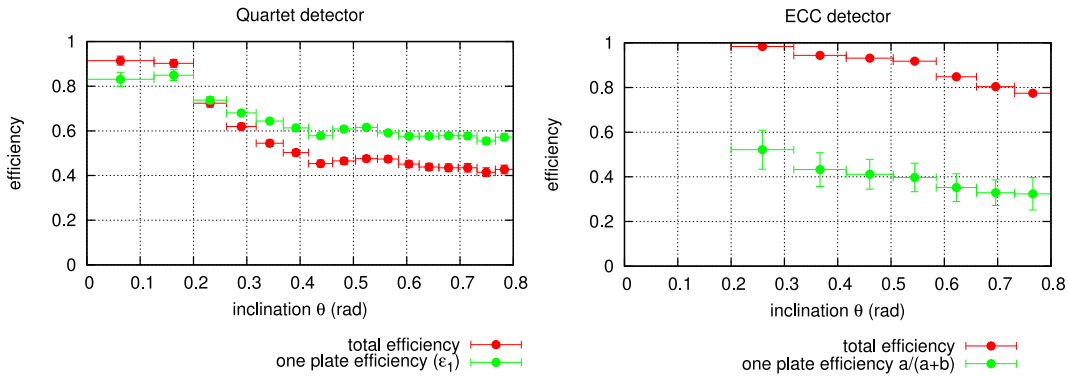


**Fig. 8.** Efficiency of signal detection as a function of track inclination  $\theta$  for the quartet detector (left panel) and ECC detector (right panel). The green circles show the efficiency for single film and the red circles show the total detection efficiency  $\epsilon^{Q,\text{ECC}}$ .

[Title Page](#)[Abstract](#)[Introduction](#)[Conclusions](#)[References](#)[Tables](#)[Figures](#)[|◀](#)[▶|](#)[◀](#)[▶](#)[Back](#)[Close](#)[Full Screen / Esc](#)[Printer-friendly Version](#)[Interactive Discussion](#)

**BG study on muogrphy**

R. Nishiyama et al.

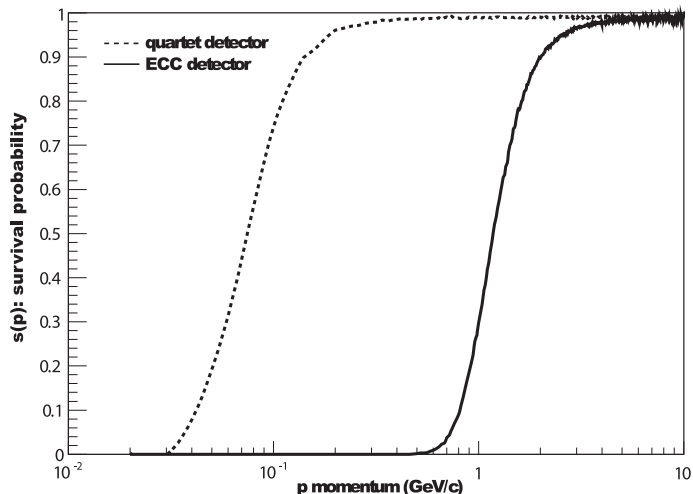


**Fig. 9.** Momentum dependence of the efficiency for the ECC detector (solid line) and quartet detector (dashed line).

[Title Page](#)[Abstract](#)[Introduction](#)[Conclusions](#)[References](#)[Tables](#)[Figures](#)[◀](#)[▶](#)[◀](#)[▶](#)[Back](#)[Close](#)[Full Screen / Esc](#)[Printer-friendly Version](#)[Interactive Discussion](#)

**BG study on muogrphy**

R. Nishiyama et al.

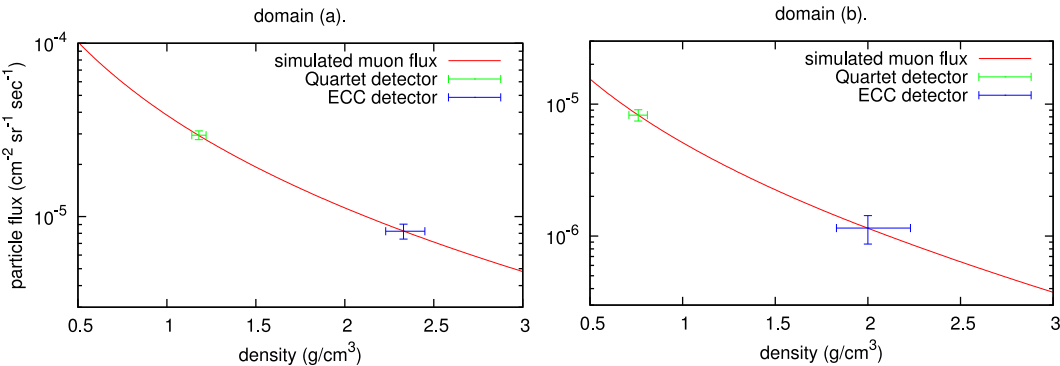


**Fig. 10.** Simulated muon flux against assumed density for two angular domains, (a): left and (b): right. The particle fluxes observed in the quartet and ECC detectors are shown by green and blue vertical error-bars ( $1\sigma$ ). The estimated density values are shown by the horizontal error-bars.

[Title Page](#)[Abstract](#)[Introduction](#)[Conclusions](#)[References](#)[Tables](#)[Figures](#)[|◀](#)[▶|](#)[◀](#)[▶](#)[Back](#)[Close](#)[Full Screen / Esc](#)[Printer-friendly Version](#)[Interactive Discussion](#)